Accelerated multi-property screening of Fe–Co–Ni alloy libraries by hyper-heuristic combinatorial flow synthesis and high-throughput spark

Journal of Materials Research and Technology 27 (2023) 2976–2988

Contents lists available at ScienceDirect

Journal of Materials Research and Technology

journal homepage: www.elsevier.com/locate/jmrt

Accelerated multi-property screening of Fe–Co–Ni alloy libraries by hyper-heuristic combinatorial flow synthesis and high-throughput spark plasma sintering

Shakti P. Padhy [a], Li Ping Tan [a,1], Vijaykumar B. Varma [a,b,1], V. Chaudhary [c,**], Z. Tsakadze [d], R.V. Ramanujan [a,*]

[a] School of Materials Science and Engineering, Nanyang Technological University, 639798, Singapore
[b] Process Modelling, Automation and Robotisation (PROMAR) Group, Materials Research & Technology Department, Luxembourg Institute of Science and Technology, Belvaux L-4422, Luxembourg
[c] Materials and Manufacture, Department of Industrial and Materials Science, Chalmers University of Technology, Göteborg, 41296, Sweden
[d] Residues and Resource Reclamation Centre (R3C), Nanyang Environment and Water Research Institute, Nanyang Technological University, 63714, Singapore

ARTICLE INFO

Keywords:
Combinatorial flow synthesis
High throughput spark plasma sintering
Multiple property assessment
Fe–Co–Ni materials library
Soft magnetic

ABSTRACT

High-throughput (HT) chemical synthesis facilitates accelerated materials discovery products. However, HT methods are limited by the need for expensive robotic systems, complicated methodology, and low yield. Hence, *we developed a hyper-heuristic combinatorial flow synthesis (HCFS) device capable of composition gradient generation and production of an adequate mass of Fe–Co–Ni alloy nanoparticles*. A library of 91 Fe–Co–Ni powder compositions was synthesized using this technique. *A high-throughput spark plasma sintering (HT-SPS) methodology, along with the die design, was developed for combinatorial screening of multiple properties*. 56 compositions were down-selected and consolidated into compositionally graded bulk samples using HT-SPS and subsequent annealing. The crystallographic, magnetic, electrical, and magnetic properties of the bulk library were assessed. The saturation magnetization (M_s) varied from 83.3 emu/g to 225.2 emu/g, coercivity (H_c) from 17.5 Oe to 78.4 Oe, resistivity (ρ) from 17.2 μΩ·cm to 986.7 μΩ·cm, and Vickers hardness (H_V) from 41.9 HV to 281.7 HV. Novel Fe–Co–Ni compositions, e.g., $Fe_{36.5}Co_{55.1}Ni_{8.4}$ and $Fe_{22.6}Co_{73.4}Ni_4$, with a promising multi-property set, were identified for the first time. This study demonstrated that promising new compositions exhibiting multi-property optimization can be successfully discovered by our hyper-heuristic combinatorial chemical synthesis methodology.

1. Introduction

Materials innovation is crucial in advancing technology and driving progress in various industries, such as healthcare, transportation, construction, and energy [1]. The current time frame from discovering and developing new materials to certification, manufacturing, and deployment is typically about 10–20 years [2,3]. In the discovery and development stage, trial-and-error experimentation and observation have been conventionally employed. A typical experimental method for synthesizing materials is the wet chemical technique. It has been employed for developing various types of materials, ranging from structural materials such as alloys [4–6] and ceramics [7,8] to functional materials such as catalytic materials [4,9], energy materials [8–11], optical materials [12,13], and magnetic materials [5,6,9]. However, the usual linear approach of "one sample at a time" wet-chemical synthesis technique cannot be used to explore the vast space of possible compositions and synthesis parameters such as the reactant concentration, temperature, time, and pH. Therefore, there is an urgent need to develop new high-throughput (HT) chemical synthesis devices to screen materials for the desired combination of properties.

In the past two decades, there has been significant progress in developing HT chemical synthesis techniques, consisting of sol-gel, hydrothermal, microwave-assisted, and laser scanning ablation. The sol-gel method was accelerated by implementing spin coating or drop

* Corresponding author.
** Corresponding author.
E-mail addresses: varunc@chalmers.se (V. Chaudhary), ramanujan@ntu.edu.sg (R.V. Ramanujan).
[1] Authors contributed equally.

https://doi.org/10.1016/j.jmrt.2023.10.124
Received 27 June 2023; Accepted 12 October 2023
Available online 15 October 2023

casting and automated robotic dispensers [14,15]. Similarly, a multi-chambered autoclave was designed for HT hydrothermal synthesis, and an automated robotic pipetting setup was implemented [16,17]. For HT microwave-assisted synthesis, two types of reactor systems were implemented – a multimode system where a multiple cavities holder was used for several reaction vessels and a monomode system where one reaction vessel is used by integrating robotics to carry out multiple reactions [18,19]. The disadvantages of these methods are their complexity, the need for large reaction or synthesis setups along with robotic systems, and limitations to explore the vast composition space. Recently, a new ultrafast HT technique, laser scanning ablation, has been implemented to rapidly synthesize nanostructured materials, including high-entropy alloys, high-entropy ceramics, carbon nanoparticles, amorphous materials, and composites [20–23]. However, the limitations of this method are the limited amount of samples produced and difficulties in removing the nanomaterials from the substrate.

The limited sample amount, the complex experimental setup, and high cost of operation has led to combinatorial continuous flow synthesis setups [24], e.g., microfluidic setups [25,26], continuous hydrothermal flow synthesis setups [27–29], and microwave-assisted continuous flow synthesis setups [30,31]. These systems have been implemented for the synthesis of metallic nanoparticles [25,26], quantum dots [25,26,29], perovskites [26,27], binary alloys [32], oxides [24,28,31], and organic compounds. A library of materials was synthesized, with various compositions, sizes, and properties, by varying the flow rates or by varying the reaction temperatures. The majority of the research on continuous flow synthesis was performed for exploring organic compounds. For metals and alloys, only a few flow synthesis studies were performed which explored a limited composition space and produced a low yield of particles. Hence, this study focused on developing a flow synthesis setup to produce a higher yield of ternary alloy particles to explore the ternary composition space and their associated structural and functional properties.

An important class of alloys are magnetic alloys which are used very widely in a variety of electromagnetic and energy conversion devices. There is an urgent need for developing efficient, high-performance, and sustainable energy-related technologies for more inclusive universal access to modern energy, keeping up with the socio-technological progress. This progress is getting hampered due to sudden reshaping of energy demand trends, more than 100 % increased energy demand in developing counties; the projected 14 % increase in global energy consumption and 300 % increase in electricity demand by 2050 [33,34]. In particular, it is critical to developing high-speed electric machines which are in high demand in various sectors such as industrial motors, renewable power generation (particularly from wind), and transportation (e.g., aerospace, naval, hybrid/electric traction) [35]. However, it is challenging to develop high-power density electric machines with increased efficiency, decreased manufacturing cost, high torque, and a lightweight design [36,37]. Magnetic alloys are a fundamental component of these machines, hence, to create next-generation electric machines for high-frequency and high torque conditions, it is necessary to develop magnetic alloy compositions with the optimal mix of functional and structural properties.

To identify suitable alloy compositions, Fe, Co, and Ni were chosen as the main constituent elements as we hypothesize that the Fe–Co–Ni ternary alloy system has promising novel alloy compositions to achieve a balanced mix of desirable values of properties. The often-antagonistic relationships of magnetic, electrical, and mechanical properties pose a challenge to find such potential compositions. The magnetic properties of saturation magnetization (M_s) and Curie temperature (T_c) depend on the composition of the alloy, e.g., with larger Ni content both M_s and T_c decrease as per the Slater-Pauling curve and the Bethe-Slater curve, respectively [38,39]. The coercivity (H_c) is observed to decrease with higher Ni content, which can be due to the low anisotropy constant of Ni, followed by that of Fe and Co [40,41]. Further, it was observed that addition of Co and Ni to Fe based alloys increases the electrical resistivity (ρ) [42]. The increase of ρ was higher when Ni was added to Fe based alloys, suggesting that comparatively higher Ni content in Fe–Co–Ni can lead to higher ρ. Moreover, Co exhibits mechanically superior properties compared to Fe and Ni [43], which suggests that comparatively high Co content might lead to better mechanical properties.

It was reported that a $Fe_{30}Co_{50}Ni_{20}$ film exhibited a high M_s of 217.2 emu/g with moderate H_c of 11 Oe and low ρ of 11 μΩ·cm. A $Fe_{15}Co_{60}Ni_{25}$ film exhibited a low H_c of 4.1 Oe with a moderate M_s of 168.7 emu/g and a moderate ρ of 22.9 μΩ·cm [44]. A $Fe_{65.5}Co_{10}Ni_{24.5}$ arc melted sample was reported to exhibit H_V of 285 HV and M_s of 225.4 emu/g [45]. Commercial $Fe_{53}Ni_{30}Co_{17}$, used mainly for glass-to-metal seals due to its good thermal expansion properties matching that of borosilicate glass and alumina ceramic, exhibits a M_s of 114.4 emu/g, H_c of 0.85 Oe, H_V of 160 HV, T_c of 703K and ρ of 43 μΩ·cm [46]. A novel alloy composition ($Fe_{32.6}Ni_{27.7}Co_{27.7}Ta_5Al_7$) with a high tensile strength of 1336 MPa, low H_c of 0.98 Oe, high ρ of 103 μΩ·cm, and low M_s of 100 emu/g was reported recently [47]. In this alloy, suitable nanoprecipitates and interfacial coherency resulted in greater hindrance to dislocation motion and a reduced pinning effect of domain wall movement, thereby increasing strength and lowering coercivity, respectively. However, M_s of this alloy is lower due to the paramagnetic nature of the precipitates [48]. The properties of these materials are summarized in Table 1. Based on the above studies, Fe–Co–Ni alloy system was chosen to study to identify potential compositions with an optimum mix of properties.

A novel hyper-heuristic combinatorial flow synthesis (HCFS) experimental device, capable of high yield, rapid, and simultaneous generation of gradient compositions by a reduction-based chemical synthesis was designed, providing a semi-automated chemical flow synthesis workflow. The HCFS platform rapidly synthesized 91 compositions of Fe–Co–Ni powder alloys by varying the flow rates of the reactants. Out of these, 56 samples were consolidated into compositionally graded bulk samples using high-throughput spark plasma sintering (HT-SPS), which were further annealed rapidly. Multiple properties for both the powder and bulk alloy libraries were quickly assessed. Finally, potential novel Fe–Co–Ni alloy compositions were identified using a screening technique. Fig. 1 shows a schematic of this high-throughput work.

2. Experimental methodology

The experimental procedure in illustrated in the flowchart (Fig. 2). The HCFS device and the experimental setup, design of experiments (DOE) with the setup, materials used for the synthesis of the Fe–Co–Ni powder alloy library, converting powder alloys into a compositionally gradient bulk alloy library using high-throughput spark plasma sintering (HT-SPS), annealing of the bulk alloy library, multiple property assessment, and screening for promising candidates are summarized in this section.

2.1. Hyper-heuristic combinatorial flow synthesis device (HCFS) device

The rapid synthesis unit (Fig. 3) consisted of three sections, an HCFS device (Fig. 3(a)), pumping system, and a collection section. The experimental setup (Fig. 3(d)) for the synthesis of Fe–Co–Ni powder

Table 1
Summary of the materials.

Material System	M_s (emu/g)	H_c (Oe)	ρ (μΩ·cm)	H_V (HV)	Ref.
$Fe_{30}Co_{50}Ni_{20}$	217.2	11	11	–	[44]
$Fe_{15}Co_{60}Ni_{25}$	168.7	4.1	22.9	–	[44]
$Fe_{65.5}Co_{10}Ni_{24.5}$	225.4	–	–	285	[45]
$Fe_{53}Ni_{30}Co_{17}$	114.4	0.85	43	160	[46]
$Fe_{32.6}Ni_{27.7}Co_{27.7}Ta_5Al_7$	100	0.98	103	–	[47]

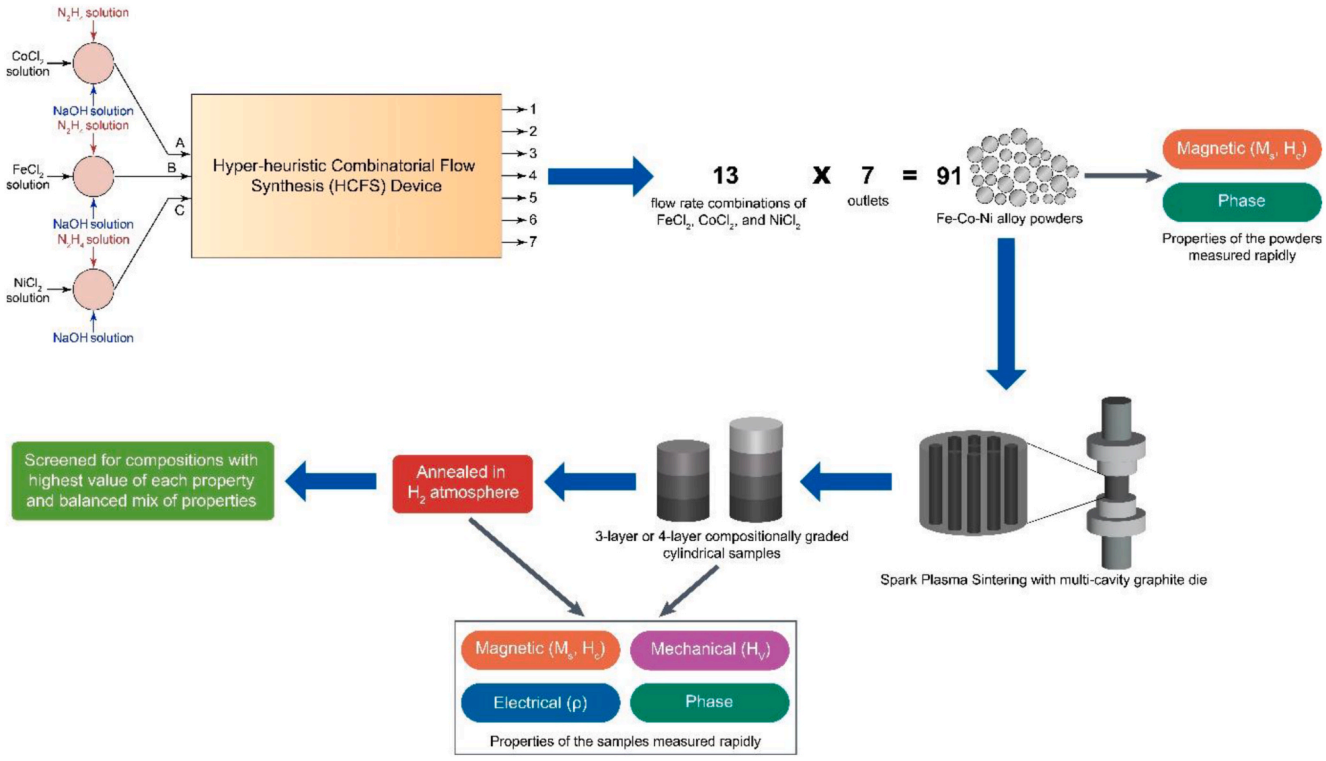

Fig. 1. Schematic of combinatorial synthesis of the Fe–Co–Ni powder and bulk alloy libraries using the hyper-heuristic combinatorial flow synthesis (HCFS) device and a multi-cavity graphite die for high-throughput spark plasma sintering (HT-SPS), respectively. Rapid assessment of the properties of powder and bulk alloy libraries are also indicated.

alloy samples was obtained by connecting the specified three sections.

A novel HCFS device for combinatorial flow synthesis of Fe–Co–Ni alloy powders was fabricated by three inlet channels (A, B, C) for reactants input flow and 7 outlet channels (O1 to O7). The device was built in chemically resistant polytetrafluoroethylene (PTFE) body, with a transparent polyethylene (PET) cover for inline imaging of combinatorial reactions. PTFE and PET were chosen as they are chemically resistant to hydrazine [49], hence, suitable to perform the selected, chemically intensive process of hydrazine reduction for Fe–Co–Ni alloys synthesis. Fig. 3(a and b) shows the design configurations and image of the fabricated device, respectively. The HCFS device's internal channel design performs the required combinatorial operation in each layer by dividing the input flows and mixing it with the other divided adjacent flow, generating the output of concentration required to synthesize different composition gradient. The device synthesizes compositions at a higher yield compared to its microfluidics counterpart [32,50–55]. The HCFS device flow rate and mixing were optimized using RGB colored water (red, green, and blue for the inlets A, B, and C, respectively), producing the mixed color spectrum at the outlets O1 to O7. We found that a minimum of 50 mL/min flow rate is required for efficient mixing, hence, suitable for rapid gradient compositions and high yield.

The pumping system consisted of 5 peristaltic pumps connected to HCFS device *via* three cross-junctions. Each cross-junction consisted of three inlet flows, one for salt solution (Co, Fe, and Ni at inlets A, B, and C, respectively), one for NaOH, and one for hydrazine, and one outlet flow connected to the HCFS device. Ethylene tetrafluoroethylene (ETFE) tubes (size: 3.175 mm outer diameter and 2.362 mm inner diameter, P/N: 1648XL, company name: IDEX, USA) connects all reactants flows by standard M6 threads with Luer lock fittings. The $FeCl_2$ solution was fed to the central inlet B to minimize the formation of oxides. Iron-rich alloys chemically synthesized by the hydrazine reduction method show oxide formation [56], hence, limiting iron-rich alloy compositions space.

We used optimization results of the HCFS setup to develop a DoE, deciding the flow rate combinations for all the input precursors with a target of $FR_{Fe} + FR_{Co} + FR_{Ni} = 300$ mL/min (where, FR_{Fe}: $FeCl_2$, FR_{Co}: $CoCl_2$, FR_{Ni}: $NiCl_2$, FR_{NaOH}: NaOH and FR_{Hyd}: N_2H_4 solutions). Table 2 describes designed experimental runs and their parameters. From experimental run 1 to 5, FR_{Co} was varied to obtain Co-rich alloys with a range of Ni and Fe content. Similarly, FR_{Ni} and FR_{Fe} was varied to obtain alloy compositions over a wide range of ternary Fe–Co–Ni compositions. About 200 mL of the resultant solution was collected from each outlet channel. The run time for collecting the stated amount of solution was in the range of 1 min 35 s to 2 min per experiment.

2.2. Synthesis of Fe–Co–Ni powder alloy library

Iron (II) chloride tetrahydrate ($FeCl_2{\cdot}4H_2O$, 98 %, CAS No. 13478-10-9), nickel (II) chloride hexahydrate ($NiCl_2{\cdot}6H_2O$, 98 %, CAS No. 7791-20-0), and cobalt (II) chloride hexahydrate ($CoCl_2{\cdot}6H_2O$, 98 %, CAS No. 7791-13-1) from Sigma Aldrich, ethanol (EtOH, 99.8 %, CAS No. 64-17-5) from Fisher Scientific, hydrazine monohydrate ($N_2H_4{\cdot}H_2O$, 80 % solution in water, CAS No. 7803-57-8) from Merck, sodium hydroxide (NaOH, CAS No. 1310-73-2) pellets from Schedelco, and deionized water (DI H_2O, Type II+, Elga) were used as received.

First, precursor solutions of 0.3 M $FeCl_2$, 0.3 M $NiCl_2$, and 0.3 M $CoCl_2$ were prepared by dissolving appropriate amounts of $FeCl_2{\cdot}4H_2O$, $NiCl_2{\cdot}6H_2O$, and $CoCl_2{\cdot}6H_2O$ in the solvent consisting of EtOH and deionized water (DIW) in the ratio of 3:1. Second, NaOH pellets were dissolved in DIW to form a 3 M NaOH solution. Finally, hydrazine was used as received for the reaction in the HCFS device. After collection of the resulting solutions from each experimental run, the solutions were left aside for approx. 3 h in glass beakers by covering their lid gently. For the solutions in which magnetic alloy (black) particles were formed, they were first separated using magnetic decantation, and then washed three times with a 95 % ethanol + 5 % methanol solution using magnetic decantation. For the solutions in which oxide (brown) particles or hydroxides are formed, there is little or no magnetic attraction, hence they

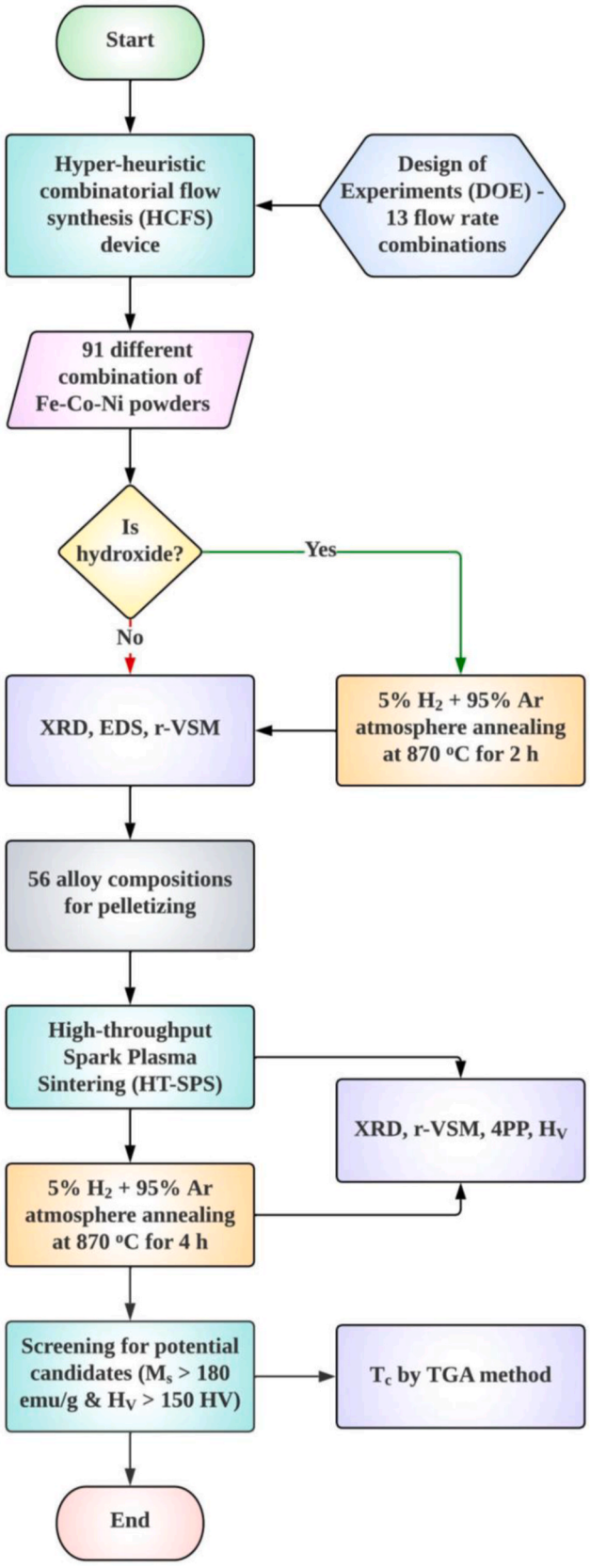

Fig. 2. Flowchart of the accelerated methodology for producing a Fe–Co–Ni bulk alloy library and rapidly assessing structural, magnetic, electrical, and mechanical properties (XRD – X-ray diffraction, EDS – Energy dispersive X-ray spectroscopy, r-VSM – rapid Vibrating Sample Magnetometer, 4 PP – Four-point probe, H_V – Vickers Hardness).

were first centrifuged at 4000 rpm for 3 min and then washed thrice with 95 % ethanol and 5 % methanol using centrifugation for the same conditions. The samples were then placed in a vacuum oven for drying. The hydroxide powder samples were then reduced in a 95 % Ar + 5 % H_2 atmosphere at 870 °C for 2 h.

2.3. Rapid screening of the Fe–Co–Ni powder alloy library

The powders, including hydroxides, were analyzed using rapid X-ray diffraction (XRD), energy dispersive X-ray spectroscopy (EDS), and vibrating sample magnetometery (VSM). Crystallographic information of the powders was determined using an automated Bruker D8 Advance diffractometer (Cu K_α radiation, $\lambda = 0.154$ nm). Elemental mapping of the powders was performed using an energy dispersive X-ray spectrometer attached to the JEOL JSM-7600F field emission scanning electron microscope (FESEM), at a rate of 2 min per sample. The magnetic properties of the powders were measured using a LakeShore Cryotronics 7400 VSM rapidly at a rate of 4 min per sample.

2.4. Compositionally graded Fe–Co–Ni bulk alloy library using HT-SPS

To accelerate the process of SPS and simultaneously consolidate powders of many alloy compositions, a graphite die with nine cavities was designed, Fig. 4(a) and (b). Compositionally graded Fe–Co–Ni bulk alloy samples were prepared using SPS by consolidating the synthesized powders as discrete layer [41,56] cylindrical samples of 8 mm diameter, as shown in Fig. 4(c). Each layer was separated by using tantalum (Ta) foil as an inert spacer. 56 alloy compositions were chosen to cover most of the composition space of the ternary diagram. SPS was performed using a Fuji Electronic Industrial SPS-211LX equipment at a vacuum level below 9 Pa. The final actual temperature was 700 °C. Thus, sintering was conducted at 700 °C for 35 min under a pressure of 40 MPa per cavity. The sintered samples were cut vertically in four sections, two sections were labelled “as-SPS”, the other two sections were annealed at 870 °C for 4 h in a 95 % Ar + 5 % H_2 atmosphere and labelled “annealed”. To increase the throughput, annealing was performed by placing two sections of two sets of compositionally graded SPS samples in the alumina crucible. The rectangular cross section samples (both as-SPS and annealed) were embedded in epoxy and used for microhardness measurements.

2.5. Rapid characterization of Fe–Co–Ni bulk alloy library

The crystal structures of as-SPS and annealed samples were determined by automated XRD using a Bruker D8 Advance diffractometer (Cu K_α radiation, $\lambda = 0.154$ nm). The magnetic properties of the samples were measured using a LakeShore Cryotronics 7400 VSM at a rate of 14 min per composition. The microhardness of the samples was measured, using a Vickers hardness tester (Future-Tech) at a load of 5 kgf, at a rate of 30 s per composition. The I–V curves of the samples were obtained using a four-point probe (4 PP) tester (Keithlink) at the rate of 2 min per composition. The ρ of the samples were calculated using the following equation [56–58]:

$$\rho = R \bullet \frac{\pi t}{\ln\left(\frac{\sinh\left(t/s\right)}{\sinh\left(t/2s\right)}\right)}$$

where R, t and s are the resistance, sample thickness and probe spacing respectively.

2.6. Screening for potential candidates

Annealed SPS samples were used for final screening of potential compositions with an optimum combination of properties. As a

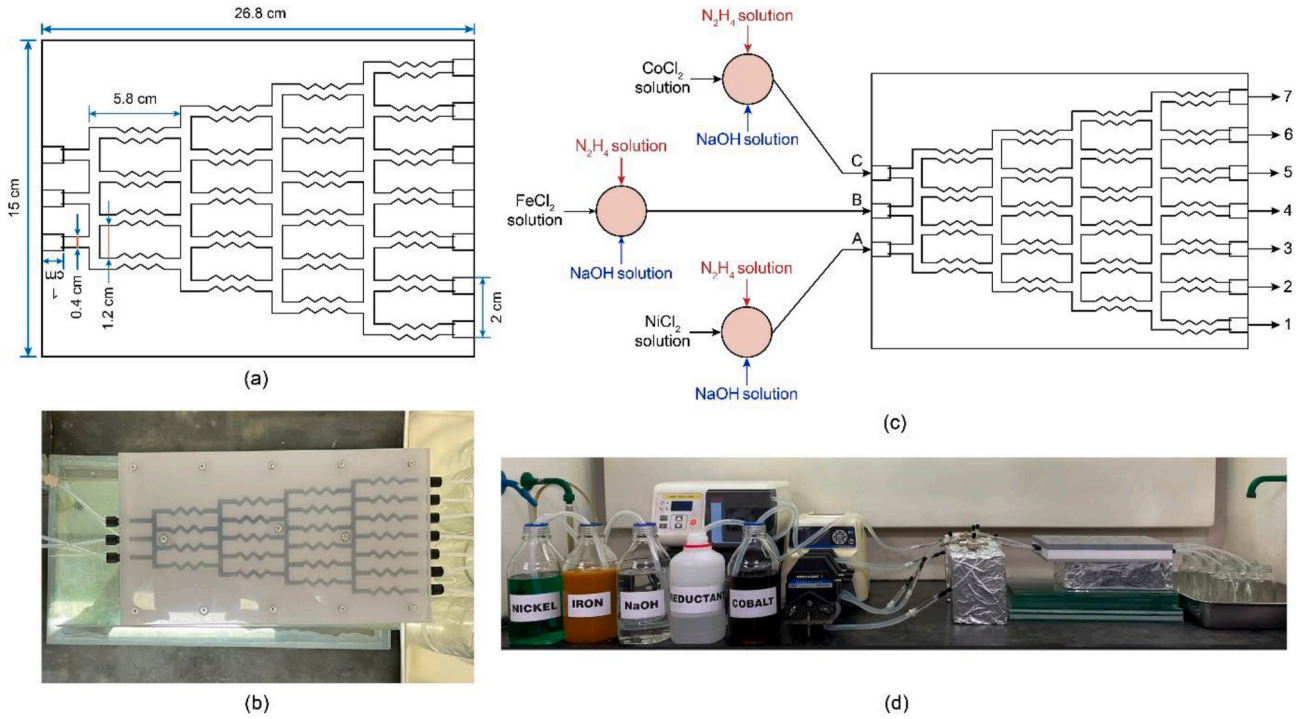

Fig. 3. (a) Design with dimensions and (b) image after fabrication of the hyper-heuristic combinatorial flow synthesis (HCFS) device. (c) Schematic representation and (d) image of the experimental setup for high-throughput (HT) synthesis of Fe–Co–Ni powder alloy library.

Table 2
Design of experiments (DoE) for synthesis of Fe–Co–Ni powder alloy library.

Experimental Run No.	Flow rate of $FeCl_2$ solution (FR_{Fe}), mL/min	Flow rate of $NiCl_2$ solution (FR_{Ni}), mL/min	Flow rate of $CoCl_2$ solution (FR_{Co}), mL/min	Flow rate of NaOH solution (FR_{NaOH}), mL/min	Flow rate of N_2H_4 solution (FR_{Hyd}), mL/min
1	100	100	100	100	240
2	90	90	120	90	240
3	80	80	140	80	240
4	110	110	80	110	240
5	120	120	60	120	240
6	90	120	90	90	240
7	80	140	80	80	240
8	110	80	110	110	240
9	120	60	120	120	240
10	120	90	90	90	240
11	140	80	80	80	240
12	80	110	110	110	240
13	60	120	120	120	240

reference, individual compositions possessing the highest M_s, lowest H_c, highest ρ, and highest H_V were identified. The following criteria for screening was used: $M_s > 80$ % of highest M_s and $H_V > 50$ % of highest H_V. After determining the compositions, the T_c of the same samples were measured by a home-built thermogravimetric analysis (TGA) setup, with a permanent magnet placed near the TGA pan, as discussed in earlier reports [41,56,59]. For TGA, TA instruments Q600 SDT was used.

3. Results and discussion

3.1. Fe–Co–Ni powder alloy library

Fig. 5 shows the 91 Fe–Co–Ni powder alloy compositions in the ternary phase diagram, obtained from a series of high-throughput experiments (HTE) using the HCFS device. Samples spanning the ternary composition space of the Fe–Co–Ni alloy can be synthesized in a semi-automated experimental setup. ***This device automatically incorporates the mixing of reactants in appropriate amounts and performs the reaction in a controlled environment with minimal human intervention***. Hence, it is referred to as hyper-heuristic combinatorial flow synthesis.

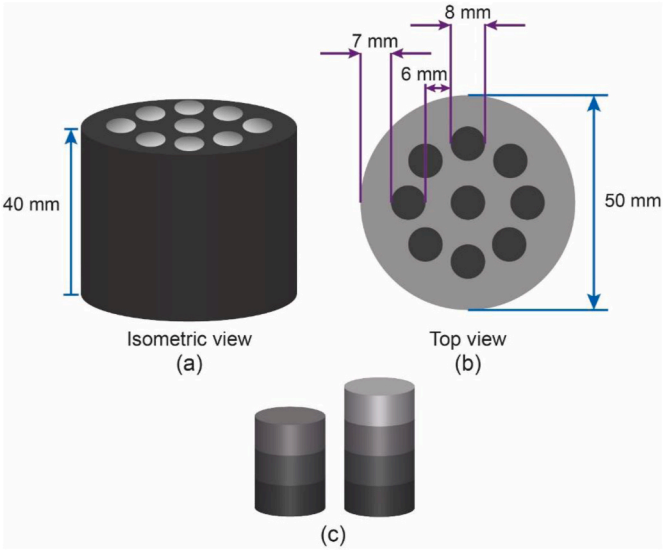

Fig. 4. (a) Isometric view and (b) Top view of the designed graphite die for HT-SPS of the synthesized Fe–Co–Ni alloy powder samples. (c) Representation of 3 layer and 4 layer compositionally graded bulk alloy samples synthesized using HT-SPS.

3.1.1. Process parameters

The Fe, Co and Ni content was determined using EDS. The composition of the powder alloys obtained from outlet 1 are Ni-rich and from outlet 7 are Co-rich, in accordance with the experimental setup shown in

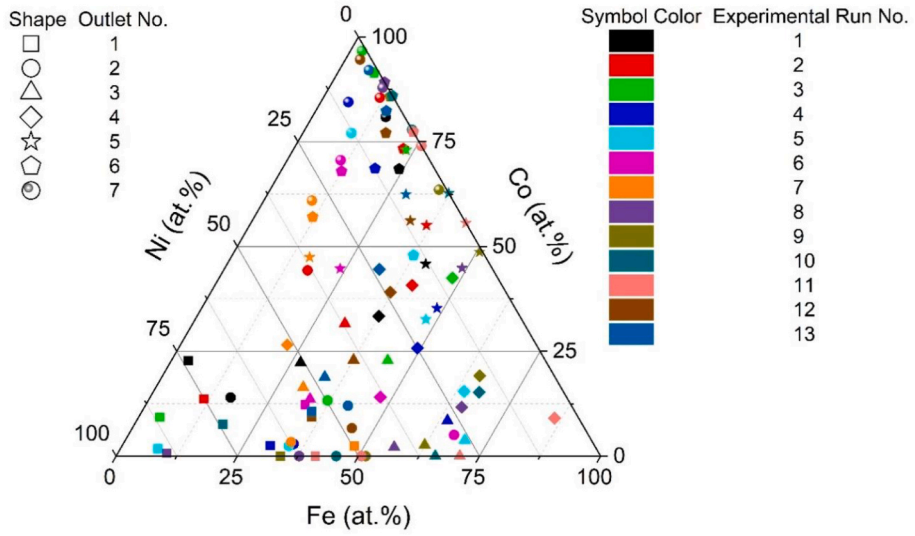

Fig. 5. Distribution of Fe–Co–Ni powder alloy library composition obtained from HT synthesis using the HCFS device. Each experimental run is denoted with a unique color as shown on the right side and the seven different alloy compositions obtained in each experimental run from the seven outlets are denoted with unique symbols as shown on the top left side.

Fig. 3(c): outlet 1 is towards the $NiCl_2$ solution and outlet 7 is towards the $CoCl_2$ solution. Powders obtained from outlets 3, 4, and 5 have a Fe content mainly between 25 and 75 at.%, along with decreasing Ni content and increasing Co content from outlet 3 to 5. Such a concentration gradient behavior of the HCFS device design is consistent with reported concentration gradients in Christmas-tree design microfluidic devices [50,51,53–55,60]. Our device and experimental setup has the uniqueness of producing higher yield compared to previously reported work on Ni–Co using a microfluidic device [32]. ***A higher yield is essential to evaluate multiple properties, samples of at least dimensions 5 mm × 5 mm × 1 mm are needed for the multiple property measurements***.

The flow rates were used to tune the concentration gradient of the solutions in the channel, resulting in the wide distribution of alloy compositions. From experimental run 1 to runs 2 and 3, FR_{Co} was increased in steps of 20 mL/min, FR_{Ni} and FR_{Fe} decreased in steps of 10

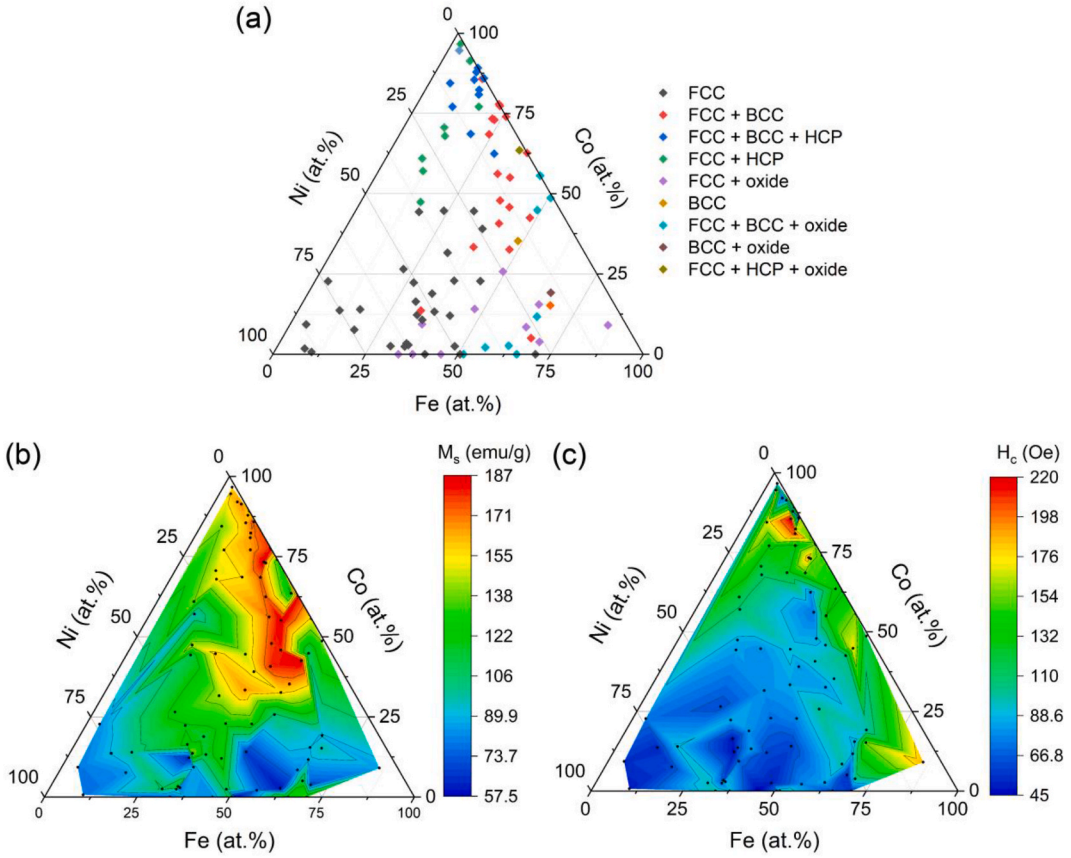

Fig. 6. (a) Phases, (b) contour plot of saturation magnetization (M_s), and (c) contour plot of coercivity (H_c) of Fe–Co–Ni powder alloy library.

mL/min, which resulted in a lower Ni and Fe content in outlets 5 to 7, enabling the synthesis of Co-rich samples. From experimental run 1 to runs 4 and 5, FR_{Co} was decreased in steps of 20 mL/min, FR_{Ni} and FR_{Fe} were increased in steps of 10 mL/min, which caused the increase in Ni and Fe content in outlets 5 to 7, enabling the synthesis of samples with greater Fe and Ni content compared to experimental runs 2 and 3. Similarly, FR_{Ni} and FR_{Fe} could be varied to obtain powder alloy compositions distributed across the maximum area of the ternary space.

3.1.2. Characterization and property evaluation

Fig. 6 shows the crystal structure, saturation magnetization (M_s), and coercivity (H_c) of the powder alloy library.

3.1.2.1. Crystal structure. In Fig. 6(a), depending on the composition, face centered cubic (FCC), body centered cubic (BCC), FCC + BCC, FCC + BCC + hexagonal closed packed (HCP), FCC + HCP, and some oxides were observed. The XRD of these powder alloy samples are presented in Figure S1 in Supporting Information (SI). Compositions with higher content of Co, Ni content <37.5 %, and Fe content <30 % showed crystal structures of either FCC + HCP, FCC + BCC + HCP, or FCC + BCC, which is consistent with the reported formation of two phases and three phases in Fe–Co–Ni nanostructured powder alloys [61]. Hence, formation of metastable phases in Co-rich ternary nanostructured alloys through this method is possible. Similarly, the compositions with higher content of Ni mainly exhibited a FCC crystal structure [61–63]. Finally, the compositions with higher content of Fe exhibited either BCC, FCC + BCC, or FCC crystal structure but had a greater tendency to form Fe_2O_3 by the reaction of Fe with the dissolved oxygen in water. Early formation of oxides of Fe is possible because of the higher reduction potential of Fe^{2+} ($E^o = -0.44$) compared to Co^{2+} ($E^o = -0.28$) and Ni^{2+} ($E^o = -0.26$) [64].

The near-equiatomic compositions of Fe–Co–Ni mainly exhibited the FCC crystal structure with some tendency to form FCC + BCC phases. This tendency increases when we move from the equiatomic region to the Co-rich region. This is partly in agreement with the phase diagram reported by Zaharov et al. [61] for Fe–Co–Ni nanostructured particles synthesized by hydrazine reduction at 90 °C. The synthesis temperature in this work was room temperature. Thus, a few of the compositions showed minority non-equilibrium phases.

3.1.2.2. Magnetic properties. The M_s of the powder alloy library was in the range of 187 emu/g to 57.5 emu/g for the compositions $Fe_{48.2}Co_{42.5}Ni_{9.3}$ and $Fe_{51.5}Ni_{48.5}$, respectively. However, the latter composition exhibited crystal structure of FCC + BCC along with a minority oxide phase. The non-oxide composition with the lowest M_s of 64.1 emu/g was $Fe_{32.9}Co_{12.2}Ni_{54.9}$. In Fig. 6(b), it can be observed that M_s decreased with higher Ni content due to the lower atomic magnetic moment of Ni ($0.6\mu_B$) compared to that of Co ($1.7\mu_B$) and Fe($2.2\mu_B$) [65]. Moreover, the region of high M_s (orange and red color region) is for the compositions with Ni content <30 %, Fe content <55 %, and Co content >30 %, which can be attributed to the enhancement of M_s by the presence of the BCC phase. The powder alloys in this region consists of BCC as one of the crystal structures, as reported previously in the Fe–Co–Ni alloy system [5,56,66–69].

Similarly, the H_c of the powder alloy library was in the range of 45 Oe to 219.4 Oe for the compositions $Fe_{45.4}Ni_{54.6}$ and $Fe_{11.7}Co_{85.5}Ni_{2.8}$, respectively. The crystal structures found in the former composition was FCC + BCC + HCP and in the latter was FCC along with oxide. The non-oxide composition with the lowest H_c was $Fe_{32.9}Co_{12.2}Ni_{54.9}$ with a value of 47 Oe, it also exhibited the lowest M_s and a crystal structure of FCC. In Fig. 6(c), it can be observed that the H_c decreases with increasing Ni content or decreasing Fe and Co content [5,66,70–72], which can be attributed to the higher anisotropy constant of Co, followed by that of Fe and finally that of Ni [40,41,73,74].

Finally, to identify compositions with an optimum combination of high M_s and lower H_c in the powder alloy library, the following constraint was applied: $M_s > 0.8 \times 187$ emu/g and $H_c < 0.3 \times 219.4$ Oe. There were only two compositions satisfying this constraint, which are $Fe_{13.7}Co_{85.8}Ni_{0.5}$ ($M_s = 175.5$ emu/g, $H_c = 63.2$ Oe) and $Fe_{6.1}Co_{92.1}Ni_{1.8}$ ($M_s = 164.2$ emu/g, $H_c = 63.8$ Oe). Another composition with M_s close to the former composition and slightly higher H_c was also identified, which is $Fe_{32.6}Co_{56.2}Ni_{11.2}$ ($M_s = 172$ emu/g, $H_c = 72.9$ Oe).

3.2. Fe–Co–Ni bulk alloy library (as-SPS)

Fig. 7 shows the crystal structure, M_s, H_c, H_V, and ρ of the as-SPS bulk alloy library. Out of the 91 powder alloy compositions, 56 compositions were chosen for HT-SPS such that these compositions cover most of the ternary composition space and have sufficient mass of powders to consolidate the powders into a bulk sample.

3.2.1. SPS process

The details of the SPS process are included in Figure S2 in SI. There, an image of the prepared SPS graphite die (from Fig. 4), its placement in the vacuum chamber of the SPS machine, and the change in SPS process parameters with time is shown. An example of a longitudinally cut sample is shown in the inset of Figure S2(c). SPS is a versatile technique, and with good control of parameters, dense samples with good mechanical properties can be obtained in the target material system [75–77]. In this work, the SPS parameters were selected to be same as that employed in our earlier work [41,56,58], while the final parameters reached were dependent on the die set and SPS equipment capability. Nevertheless, these conditions allowed sufficiently dense samples to be fabricated. The shrinkage of samples during SPS is briefly discussed in SI as well. The porosity information of a selected sample, as SPS and after annealing, is presented and discussed in Figure S3 in SI.

Also, as inert Ta foils are used as spacers between each layer, no interdiffusion between the layers occurred. This is supported by further characterization in Table S1, Figures S4, S5 and S6 (consisting of SEI, EDS and XRD), which shows no penetration of the layers into one another. Use of SPS in a similar fashion, but without the inert layer, has been reported by Shichalin et al. [78], to form functionally graded materials by purposefully joining different metals. This approach is useful for fabricating materials with different compositions (and in turn site-specific material properties) [41].

3.2.2. Crystal structure

In Fig. 7(a), it can be observed that the HCP crystal structure in Co-rich alloys (Co content >50 %) was absent, except for two alloys which have very high Co content. The majority of the ternary compositions exhibited the FCC crystal structure. Unlike powder alloys, the Fe-rich (Fe content >50 %) as-SPS bulk alloys exhibited the FCC or FCC + BCC crystal structures and not the BCC crystal structure. Interestingly, for 50 % < Fe content <65 %, the crystal structure was FCC and for Fe content >65 %, the crystal structure was FCC + BCC. This suggests that for high Fe content, the BCC structure may occur, this structure is the stable phase for high Fe content [66]. Further, the majority phase in alloys with higher Ni content in near-equiatomic Fe–Co–Ni exhibited the FCC crystal structure, as reported earlier [5,56,66]. Some of the alloy compositions exhibited some oxide formation after SPS. The compositionally graded SPS samples were annealed in hydrogen atmosphere to remove the oxide phases [56,79], all the properties were then evaluated.

After SPS, most of the higher Co content powder alloys, consisting of HCP as one of the crystal structures, were transformed into pelletized bulk alloys consisting of FCC and FCC + BCC crystal structures. However, the $Fe_{2.4}Co_{96.7}Ni_{0.9}$ and $Fe_{11.1}Co_{87.9}Ni_1$ compositions consisted of FCC + HCP crystal structures. Further, $Fe_{34.4}Co_{2.4}Ni_{63.2}$ and $Fe_{17.4}Co_{44.3}Ni_{38.3}$ exhibited the FCC + BCC crystal structures after SPS, compared to the FCC crystal structure in the powders. These two compositions stand out compared to others as neighboring compositions show only the FCC crystal structure. This may be attributed to the

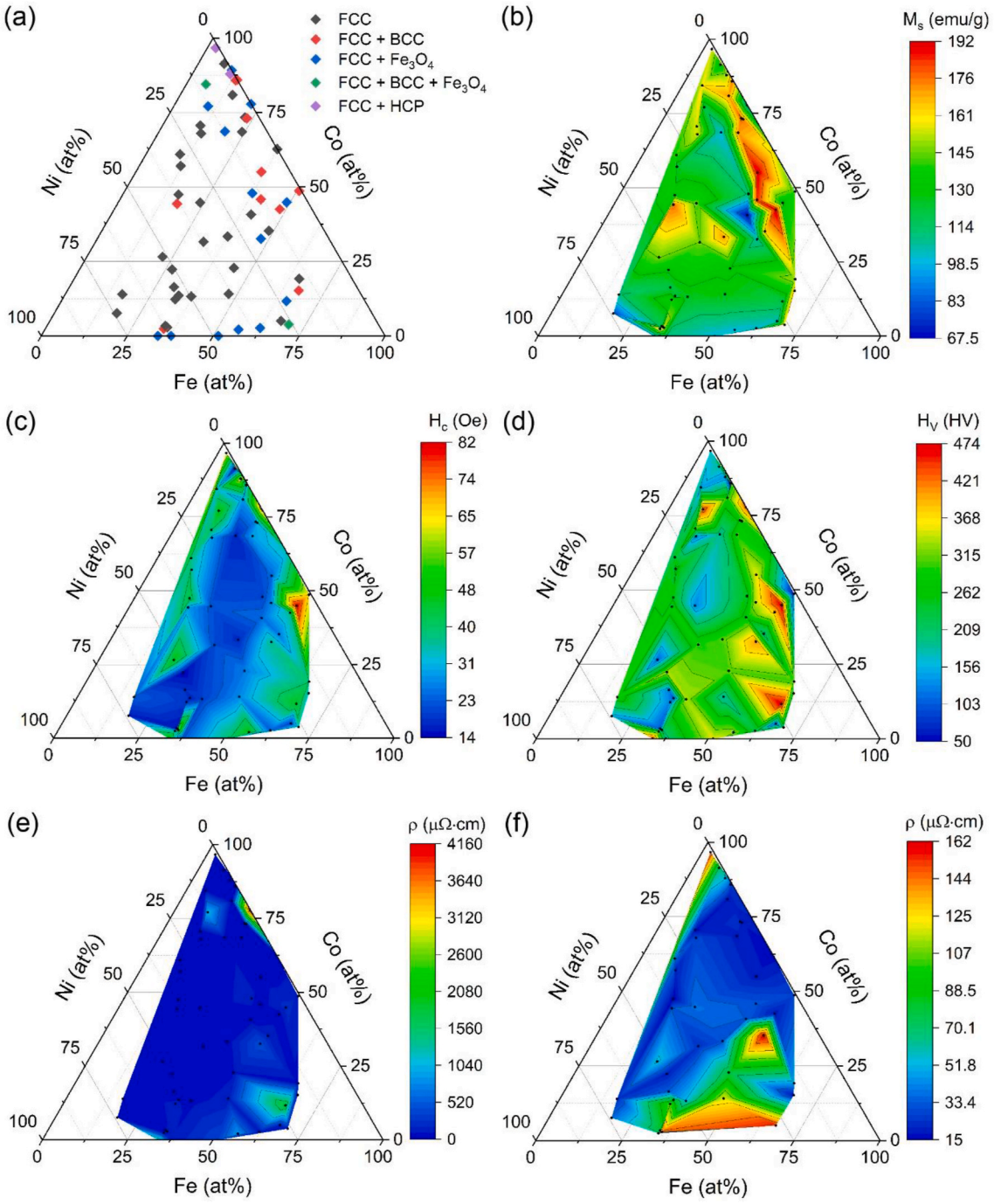

Fig. 7. (a) Composition and phases, contour plot of (b) saturation magnetization (M_s), and (c) coercivity (H_c), (d) Vickers hardness (H_V), (e) electrical resistivity (ρ), and (f) ρ excluding compositions with oxide phases of as-SPS Fe–Co–Ni bulk alloy library. (f) Is plotted to display greater contrast of ρ values of as-SPS samples.

metastable state of the FCC and BCC crystal structures in the two compositions.

3.2.2.1. Magnetic properties. The M_s of the as-SPS bulk alloy library was in the range of 191.3 emu/g to 67.9 emu/g for the compositions $Fe_{48.2}Co_{42.5}Ni_{9.3}$ and $Fe_{40.7}Co_{40.8}Ni_{18.5}$, respectively. The M_s of the $Fe_{40.7}Co_{40.8}Ni_{18.5}$ powder alloy was 179.4 emu/g and the crystal structures were FCC + BCC. However, after SPS, the crystal structure of the alloy was changed to FCC, resulting in a decrease of M_s, which shows the influence of the BCC crystal structure in enhancing M_s [5,56,66–69]. The second lowest value of M_s was 79.7 emu/g for the composition $Fe_{18.2}Co_{7.6}Ni_{74.2}$, which can attributed to the fact that Ni has the lowest atomic magnetic moment among the three elements [65]. In Fig. 7(b), it can be observed that the region of high M_s is similar to that of the powder alloy library but with a narrower spread. It now includes of $Fe_{17.4}Co_{44.3}Ni_{38.3}$, whose crystal structure changed after SPS from FCC to FCC + BCC.

In Fig. 7(c), the H_c values of the as-SPS bulk alloy library compositions were in the range of 14.5 Oe to 82.3 Oe for the compositions $Fe_{26.9}Co_{22.3}Ni_{50.8}$ and $Fe_{49}Co_{44.9}Ni_{6.1}$, respectively. The crystal structure of the former composition was FCC and of the latter was FCC + an oxide phase. The non-oxide composition with the highest H_c was $Fe_{50.7}Co_{48.7}Ni_{0.6}$ with a value of 65 Oe, which exhibited FCC + BCC crystal structures. The compositions $Fe_{2.4}Co_{96.7}Ni_{0.9}$ and $Fe_{11.1}Co_{87.9}Ni_1$

which exhibited FCC + HCP crystal structures had H_c values of 64.5 and 62.2 Oe, which can be attributed to the high anisotropy constant of Co [41,73,74].

3.2.2.2. Hardness. In Fig. 7(d), the H_V of the as-SPS bulk alloy library was found to be in the range of 473.8 HV to 51 HV for the compositions $Fe_{65.5}Co_{11.7}Ni_{22.8}$ and $Fe_{13.7}Co_{85.8}Ni_{0.5}$, respectively. The crystal structure of the former composition was FCC along with oxide and of the latter was FCC + BCC. The non-oxide composition with highest H_V was $Fe_{48.2}Co_{42.5}Ni_{9.3}$ with 380.9 HV, which also exhibited the highest M_s and crystal structures of FCC + BCC. Further, the composition with second highest H_V was $Fe_{36.5}Co_{55.1}Ni_{8.4}$ with 380.9 Oe which also exhibited the second highest M_s of 190.9 emu/g and crystal structures of FCC + BCC. The H_c for these two compositions were 36.9 Oe and 23.9 Oe, respectively.

3.2.2.3. Resistivity. In Fig. 7(e), the ρ of the as-SPS bulk alloy library was in the range of 4153.4 μΩ·cm to 15.2 μΩ·cm for the compositions $Fe_{22.1}Co_{77.9}$ and $Fe_{16.2}Co_{47.4}Ni_{36.4}$, respectively. The crystal structure of the former composition was FCC, along with a minority oxide phase and of the latter was FCC. Due to the presence of the oxides, some of the SPS samples exhibited very high ρ and it is challenging to visualize the distribution of ρ in relation with composition. Therefore, the contour graph of ρ for the compositions without the oxide phases was plotted and is shown in Fig. 7(f).

The non-oxide composition with the highest ρ was $Fe_{48.6}Co_{32.3}Ni_{16.1}$

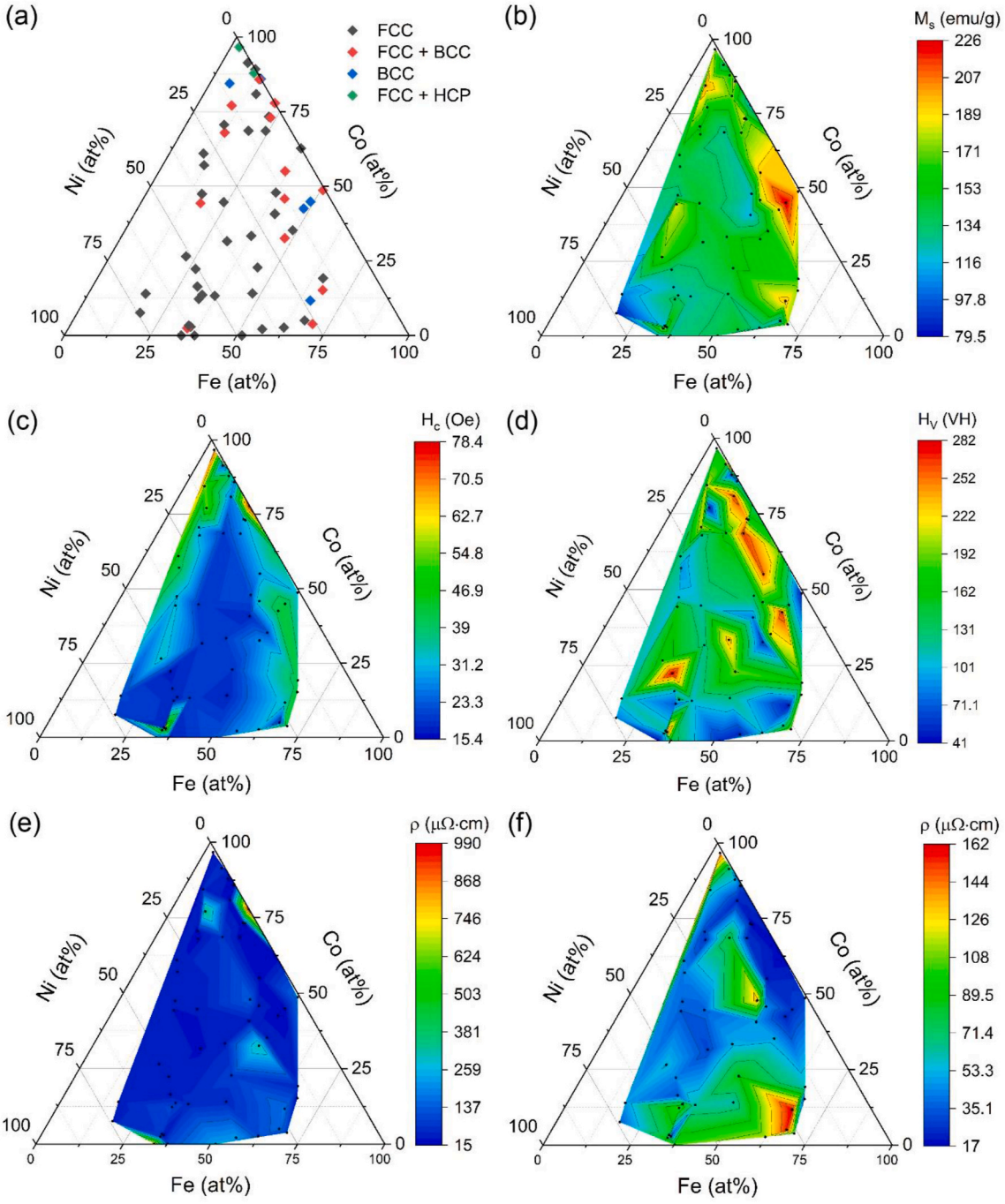

Fig. 8. (a) Composition and phases, contour plot of (b) saturation magnetization (M_s), and (c) coercivity (H_c), (d) Vickers hardness (H_V), (e) electrical resistivity (ρ), and (f) ρ excluding compositions with greater than 200 μΩ·cm. (f) Is plotted to display greater contrast of ρ values of annealed samples.

with a value of 161.9 μΩ·cm, which exhibited M_s = 162.1 emu/g, H_c = 25.8 Oe, and H_V = 193.8 HV. Moreover, when a screening criterion of $M_s > 0.8 \times 191.3$ emu/g, $\rho > 0.5 \times 161.9$ μΩ·cm, and $H_V > 0.5 \times 380.9$ HV was applied to find the as-SPS composition with an optimum combination of properties, this was the only one composition identified. A slightly less strict constraint was also applied, i.e., $M_s > 0.8 \times 191.3$ emu/g, $\rho > 0.3 \times 161.9$ μΩ·cm, and $H_V > 0.5 \times 380.9$ HV, to identify other potential compositions. Only one composition was identified – $Fe_{34.4}Co_{2.4}Ni_{63.2}$ which exhibited M_s = 163.8 emu/g, H_c = 35.7 Oe, ρ = 69.3 μΩ·cm and H_V = 278.6 HV with FCC + BCC crystal structure.

3.3. Fe–Co–Ni bulk alloy library (annealed)

Fig. 8 shows the crystal structure, M_s, H_c, H_V, ρ and ρ of the compositions of the annealed bulk alloy library with $\rho < 200$ μΩ·cm. After annealing, the oxide phase is completely removed from the SPS samples. EDS is done on a selected sample to show the homogeneity of the sample after annealing and is presented in SI Figure S7.

3.3.1. Crystal structure

In Fig. 8(a), the two compositions, $Fe_{2.4}Co_{96.7}Ni_{0.9}$ and $Fe_{11.1}Co_{87.9}Ni_1$, which exhibited the FCC + HCP crystal structures after SPS, exhibited the same crystal structure after annealing. Further, the Co-rich compositions exhibited FCC + BCC crystal structures after annealing, as compared to the FCC crystal structure before annealing. Also, $Fe_{5.7}Co_{84.4}Ni_{9.9}$ and $Fe_{14}Co_{86}$ exhibited the BCC crystal structure after annealing, compared to FCC + BCC before annealing. This shows the metastability of FCC, BCC, and HCP in Co-rich alloys prepared *via* the hydrazine reduction method, as reported previously [61]. Further, it can be observed that Fe-rich and Fe–Co rich compositions after annealing exhibited a mix of FCC, FCC + BCC and BCC crystal structures. These results are broadly in agreement with the crystal structures obtained using other techniques, e.g., hydrazine reduction and SPS [56], additive manufacturing [66], electroplating [80], and sputtering [44, 72].

3.3.2. Magnetic properties

In Fig. 8(b), the M_s of the annealed bulk alloy library was in the range of 225.2 emu/g to 83.3 emu/g for the compositions $Fe_{49}Co_{44.9}Ni_{6.1}$ and $Fe_{18.2}Co_{7.6}Ni_{74.2}$, respectively. The M_s of the $Fe_{49}Co_{44.9}Ni_{6.1}$ as-SPS alloy was 128.6 emu/g with a crystal structure of FCC along with some oxide phase. After annealing, the crystal structure of the alloy was BCC which again shows the influence of BCC in enhancing M_s. The composition $Fe_{48.2}Co_{42.5}Ni_{9.3}$, which exhibited the highest M_s of 191.3 emu/g for as-SPS condition, after annealing exhibited M_s of 187.7 emu/g, retaining the same crystal structures of FCC + BCC. Also, it was observed that the samples consisting of oxide phase before annealing exhibited comparatively higher M_s after annealing. For e.g., $Fe_{5.7}Co_{84.4}Ni_{9.9}$ exhibited an M_s of 160.4 emu/g with mixed crystal structures of FCC + BCC + Fe_3O_4 before annealing. After annealing, it exhibited an M_s of 200.9 emu/g with a crystal structure of BCC.

In Fig. 8(c), the H_c of the annealed bulk alloy library was in the range of 17.5 Oe to 78.4 Oe for the compositions $Fe_{26.9}Co_{22.3}Ni_{50.8}$ and $Fe_{22.1}Co_{77.9}$, respectively. $Fe_{26.9}Co_{22.3}Ni_{50.8}$ exhibited the lowest H_c (14.5 Oe) in as-SPS bulk alloy library as well. After annealing, the H_c increased by 3 Oe and the crystal structure remained the same, i.e., FCC. It can be observed that the H_c increases for larger Co and Fe content or lower Ni content, as explained in Section 3.1.

3.3.3. Hardness

In Fig. 8(d), the H_V of the annealed bulk alloy library was in the range of 281.7 HV to 41.9 HV for the compositions $Fe_{26.9}Co_{22.3}Ni_{50.8}$ and $Fe_{33.9}Ni_{66.1}$, respectively. $Fe_{26.9}Co_{22.3}Ni_{50.8}$ exhibited a combination of lowest H_c and highest H_V with a crystal structure of FCC, M_s of 132.2 emu/g and ρ of 42.4 μΩ·cm. $Fe_{33.9}Ni_{66.1}$ before annealing exhibited a crystal structure of FCC along with some oxide phase. After annealing, the oxide phase is removed which could have caused porosity in the sample, resulting in the low hardness of the composition.

3.3.4. Resistivity

In Fig. 8(e), the ρ of the annealed bulk alloy library was in the range of 986.7 μΩ·cm to 17.2 μΩ·cm for the compositions $Fe_{22.1}Co_{77.9}$ and $Fe_{37.3}Co_{62.7}$ respectively. $Fe_{16.2}Co_{47.4}Ni_{36.4}$, which exhibited lowest ρ (15.2 μΩ·cm) in the as-SPS bulk alloy library, exhibited a ρ of 37.2 μΩ·cm. $Fe_{22.1}Co_{77.9}$ exhibited the highest ρ for both the as-SPS and the annealed bulk alloy library. The crystal structure for this composition in the as-SPS sample was FCC along with oxide and in the annealed sample was FCC + BCC. As mentioned above, annealing can cause porosity in the sample after oxide removal, which may be the reason for such high ρ [56].

To clearly visualize the distribution of ρ in relation with composition, a contour graph of ρ was plotted with the compositions which exhibited $\rho < 200$ μΩ·cm, as shown in Fig. 8(f). In Fig. 8(f), the composition with the highest ρ was $Fe_{65.5}Co_{11.7}Ni_{22.8}$ with a value of 161.6 μΩ·cm. This composition was chosen as the composition with highest ρ for comparison with the screened potential compositions as this composition is close to the previously reported composition $Fe_{54}Co_{17}Ni_{29}$ synthesized *via* hydrazine reduction and SPS which exhibited high ρ [56].

3.4. Identification of promising compositions

Among the 56 Fe–Co–Ni annealed alloy compositions, the composition with the highest M_s ($Fe_{49}Co_{44.9}Ni_{6.1}$, 225.2 emu/g), lowest H_c and highest H_V ($Fe_{26.9}Co_{22.3}Ni_{50.8}$, 17.5 Oe, 281.7 HV), and highest ρ ($Fe_{65.5}Co_{11.7}Ni_{22.8}$, 161.56 μΩ·cm) were selected. Additionally, using the earlier mentioned screening criterion in Section 2.6, M_s > 80 % of highest M_s (M_s > 180 emu/g) and H_V > 50 % of highest H_V (H_V > 150 HV), six more compositions were selected. All of these compositions are tabulated in Table 3 below with their properties, including the measured T_c. The reason for choosing the annealed bulk alloy library is the oxide-free samples, making this library more relevant for electric machines applications.

From the screened compositions, the three compositions with the highest M_s, lowest H_c and highest H_V, highest ρ, three other compositions with a good balance of multiple properties are chosen (highlighted in bold in Table 3) for comparison. The field dependence of magnetization for the 6 samples highlighted in bold in Table 3 are shown in SI Figure S8. Fig. 9 shows the donut heatmap of these 9 compositions with their properties. The compositions $Fe_{36.5}Co_{55.1}Ni_{8.4}$ and $Fe_{22.6}Co_{73.4}Ni_4$ were chosen due to their combination of high H_V, moderately low H_c, high M_s and comparatively high values of T_c. Finally, the composition $Fe_{5.7}Co_{84.4}Ni_{9.9}$ was chosen as it exhibited a combination of high M_s, high ρ, comparatively high H_V, and T_c value greater than 800 °C.

The property contour maps of the Fe–Co–Ni ternary composition space, the screened compositions, and the radial heatmap showing the

Table 3
Screened compositions with highest M_s, lowest H_c, highest H_V, highest ρ, and combination of M_s > 180 emu/g and H_V > 150 HV.

Composition	Crystal structure	M_s (emu/g)	H_c (Oe)	T_c (°C)	ρ (μΩ·cm)	H_V (HV)
$Fe_{49}Co_{44.9}Ni_{6.1}$	BCC	**225.2**	42.7	927.2	26.35	127.3
$Fe_{26.9}Co_{22.3}Ni_{50.8}$	FCC	132.2	**17.5**	718.1	42.39	**281.7**
$Fe_{65.5}Co_{11.7}Ni_{22.8}$	BCC	194.7	33.4	724	**161.56**	47.6
$Fe_{17.4}Co_{44.3}Ni_{38.3}$	FCC + BCC	182.1	31.7	715.7	34.99	156.1
$Fe_{36.5}Co_{55.1}Ni_{8.4}$	FCC + BCC	192.9	28.9	881.7	22.42	253.7
$Fe_{22.6}Co_{73.4}Ni_4$	FCC	183	28.6	983.6	24.83	238.7
$Fe_{48.2}Co_{42.5}Ni_{9.3}$	BCC	187.7	41.6	899.4	22.75	266.7
$Fe_{5.7}Co_{84.4}Ni_{9.9}$	BCC	200.9	54.8	820	58.41	205.6
$Fe_{37.3}Co_{62.7}$	FCC	192.2	39.8	1040	17.24	188.8

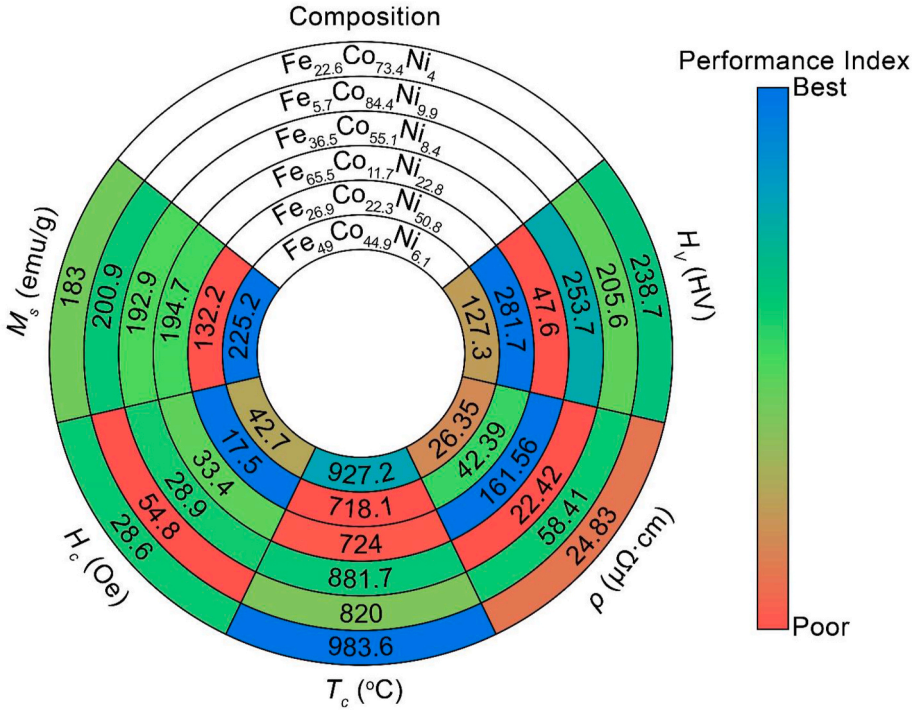

Fig. 9. Radial heatmap of consolidated potential compositions and their properties of annealed SPS Fe–Co–Ni alloy library. Notation: saturation magnetization (M_s), coercivity (H_c), Curie temperature (T_c), electrical resistivity (ρ), Vickers hardness (H_V).

properties of potential compositions are useful to select new compositions satisfying a variety of performance metrics. The identified compositions are promising for electric machine applications.

4. Conclusions

Fe–Co–Ni alloy libraries in the form of powder and bulk has been developed for the first time by a ***novel hyper-heuristic combinatorial flow synthesis (HCFS) device capable of programmable automated closed-loop rapid materials synthesis***, relevant to accelerated materials discovery. We also developed a ***high-throughput spark plasma sintering technique providing a consolidated gradient bulk alloy for rapid characterization and property evaluation***. HCFS device performed rapid, high-throughput, combinatorial synthesis providing binary and ternary alloy library of 91 compositions by the developed efficient design of experiments. The magnetic properties, saturation magnetization and coercivity, of the powder alloy library were measured rapidly and plotted on the Fe–Co–Ni ternary diagram.

Further, powders of selected 56 alloy compositions were consolidated into compositionally graded bulk alloys using high-throughput SPS. These bulk alloys were further annealed in hydrogen atmosphere. The M_s, H_c, ρ, and H_V of both the SPS and annealed bulk alloys were plotted on the Fe–Co–Ni ternary diagram.

After annealing, alloy compositions with the highest M_s ($Fe_{49}Co_{44.9}Ni_{6.1}$, 225.2 emu/g), lowest H_c and highest H_V ($Fe_{26.9}Co_{22.3}Ni_{50.8}$, 17.5 Oe, 281.7 HV), and highest ρ ($Fe_{65.5}Co_{11.7}Ni_{22.8}$, 161.56 μΩ·cm) were identified. Finally, a screening criterion of $M_s > 80$ % of highest M_s ($M_s > 180$ emu/g) and $H_V > 50$ % of highest H_V ($H_V > 150$ HV) was implemented and 6 compositions were identified. T_c measurements of all these compositions were performed and compared.

Consequently, three new compositions with an optimum combination of properties were identified for electric machine applications. As an example, $Fe_{36.5}Co_{55.1}Ni_{8.4}$ exhibits M_s of 192.9 emu/g, H_c of 28.9 Oe, T_c of 881.7 °C, ρ of 22.4 μΩ·cm and hardness of 253.7 HV. Hence, we demonstrated for the first time, a feedback-loop controlled accelerated materials discovery capabilities of HCFS device integrated with high-throughput SPS technique to produce structural, magnetic, electrical, and mechanical properties of Fe–Co–Ni alloys for current and future electrical machines.

Declaration of competing interest

The authors declare that they have no known competing financial interests or personal relationships that could have appeared to influence the work reported in this paper.

Acknowledgement

This work is supported by the AME Programmatic Fund by the Agency for Science, Technology and Research, Singapore under Grant No. A1898b0043 and Production Area of Advance (AoA) at Chalmers University of Technology. We would like to acknowledge the Facility for Analysis, Characterization, Testing and Simulation, Nanyang Technological University, Singapore, for use of their electron microscopy, EDS, X-ray facilities.

Appendix A. Supplementary data

Supplementary data to this article can be found online at https://doi.org/10.1016/j.jmrt.2023.10.124.

References

[1] Moskowitz SL. The advanced materials revolution: technology and economic growth in the age of globalization. John Wiley & Sons; 2014.
[2] Tabor DP, Roch LM, Saikin SK, Kreisbeck C, Sheberla D, Montoya JH, et al. Accelerating the discovery of materials for clean energy in the era of smart automation. Nat Rev Mater 2018;3:5–20.
[3] Kalidindi SR, Medford AJ, McDowell DL. Vision for data and informatics in the future materials innovation ecosystem. JOM 2016;68:2126–37.
[4] Al Zoubi W, Putri RAK, Abukhadra MR, Ko YG. Recent experimental and theoretical advances in the design and science of high-entropy alloy nanoparticles. Nano Energy 2023;110:108362.

[5] Reddy GS, Sahu SR, Prakash R, Jagannatham M. Synthesis of cobalt-rich alloys with high saturation magnetization: a novel synthetic approach by hydrazine reduction method. Results Phys 2019;12:652–61.
[6] Rajeevan V, Justin Joseyphus R. Structural and magnetic properties of Ni substituted FeCo alloy obtained through polyol process. J Magn Magn Mater 2022;563:170016.
[7] Kousar T, Aadil M, Zulfiqar S, Warsi MF, Ejaz SR, Elnaggar AY, et al. Wet-chemical synthesis of nanostructured Ce-doped mixed metal ferrites for the effective removal of azo dyes from industrial discharges. Ceram Int 2022;48:11858–68.
[8] Waetzig K, Rost A, Heubner C, Coeler M, Nikolowski K, Wolter M, et al. Synthesis and sintering of Li1.3Al0.3Ti1.7(PO4)3 (LATP) electrolyte for ceramics with improved Li+ conductivity. J Alloys Compd 2020;818:153237.
[9] Diodati S, Walton RI, Mascotto S, Gross S. Low-temperature wet chemistry synthetic approaches towards ferrites. Inorg Chem Front 2020;7:3282–314.
[10] Zhao X, Zheng Y, Dai H, Yang J, Chen Q, Zhou J, et al. Wet-Chemistry: a useful tool for deriving metal–organic frameworks toward supercapacitors and secondary batteries. Adv Mater Interfac 2022;9:2102595.
[11] Wang C, Liang J, Luo J, Liu J, Li X, Zhao F, et al. A universal wet-chemistry synthesis of solid-state halide electrolytes for all-solid-state lithium-metal batteries. Sci Adv 2021;7:eabh1896.
[12] Anwar S, Ding H, Xu M, Hu X, Li Z, Wang J, et al. Recent advances in synthesis, optical properties, and biomedical applications of carbon dots. ACS Appl Bio Mater 2019;2:2317–38.
[13] Mayer M, Schnepf MJ, König TAF, Fery A. Colloidal self-assembly concepts for plasmonic metasurfaces. Adv Opt Mater 2019;7:1800564.
[14] Cong P, Dehestani A, Doolen R, Giaquinta DM, Guan S, Markov V, et al. Combinatorial discovery of oxidative dehydrogenation catalysts within the Mo-V-Nb-O system. Proc Natl Acad Sci USA 1999;96:11077–80.
[15] Kim C-H. Synthesis of $ZrTiO_4$ and $Ta_2Zr_6O_{17}$ films by composition-combinatorial approach through surface sol-gel method and their dielectric properties. Bull Kor Chem Soc 2007;28:1463–6.
[16] Stock N, Bein T. High-throughput synthesis of phosphonate-based inorganic–organic hybrid compounds under hydrothermal conditions. Angew Chem Int Ed 2004;43:749–52.
[17] Tompos A, Sanchez-Sanchez M, Végvári L, Szijjártó GP, Margitfalvi JL, Trunschke A, et al. Combinatorial optimization and synthesis of multiple promoted MoVNbTe catalysts for oxidation of propane to acrylic acid. Catal Today 2021;363:45–54.
[18] Nassr ABAA, Sinev I, Pohl M-M, Grunert W, Bron M. Rapid microwave-assisted polyol reduction for the preparation of highly active PtNi/CNT electrocatalysts for methanol oxidation. ACS Catal 2014;4:2449–62.
[19] Sandström R, Gracia-Espino E, Hu G, Shchukarev A, Ma J, Wågberg T. Yttria stabilized and surface activated platinum (PtxYOy) nanoparticles through rapid microwave assisted synthesis for oxygen reduction reaction. Nano Energy 2018;46:141–9.
[20] Wang B, Wang C, Yu X, Cao Y, Gao L, Wu C, et al. General synthesis of high-entropy alloy and ceramic nanoparticles in nanoseconds. Nature Synthesis 2022;1:138–46.
[21] Yogesh GK, Shuaib EP, Kalai Priya A, Rohini P, Anandhan SV, Krishnan UM, et al. Synthesis of water-soluble fluorescent carbon nanoparticles (CNPs) from nanosecond pulsed laser ablation in ethanol. Opt Laser Technol 2021;135:106717.
[22] Bag S, Baksi A, Wang D, Kruk R, Benel C, Chellali MR, et al. Combination of pulsed laser ablation and inert gas condensation for the synthesis of nanostructured nanocrystalline, amorphous and composite materials. Nanoscale Adv 2019;1:4513–21.
[23] Lin Z, Yue J, Liang L, Tang B, Liu B, Ren L, et al. Rapid synthesis of metallic and alloy micro/nanoparticles by laser ablation towards water. Appl Surf Sci 2020;504:144461.
[24] Liu Z, Zhu J, Wakihara T, Okubo T. Ultrafast synthesis of zeolites: breakthrough, progress and perspective. Inorg Chem Front 2019;6:14–31.
[25] Volk AA, Epps RW, Abolhasani M. Accelerated development of colloidal nanomaterials enabled by modular microfluidic reactors: toward autonomous robotic experimentation. Adv Mater 2021;33:2004495.
[26] Nette J, Howes PD, deMello AJ. Microfluidic synthesis of luminescent and plasmonic nanoparticles: fast, efficient, and data-rich. Adv Mater Technol 2020;5:2000060.
[27] Groves AR, Ashton TE, Darr JA. High throughput synthesis and screening of oxygen reduction catalysts in the MTiO3 (M = Ca, Sr, Ba) perovskite phase diagram. ACS Comb Sci 2020;22:750–6.
[28] Howard DP, Marchand P, McCafferty L, Carmalt CJ, Parkin IP, Darr JA. High-throughput continuous hydrothermal synthesis of transparent conducting aluminum and gallium Co-doped zinc oxides. ACS Comb Sci 2017;19:239–45.
[29] Baragau I-A, Lu Z, Power NP, Morgan DJ, Bowen J, Diaz P, et al. Continuous hydrothermal flow synthesis of S-functionalised carbon quantum dots for enhanced oil recovery. Chem Eng J 2021;405:126631.
[30] Morschhäuser R, Krull M, Kayser C, Boberski C, Bierbaum R, Püschner PA, et al. Microwave-assisted continuous flow synthesis on industrial scale. Green Process Synth 2012;1:281–90.
[31] Nikam AV, Dadwal AH. Scalable microwave-assisted continuous flow synthesis of CuO nanoparticles and their thermal conductivity applications as nanofluids. Adv Powder Technol 2019;30:13–7.
[32] Hu Y, Liu B, Wu Y, Li M, Liu X, Ding J, et al. Facile high throughput wet-chemical synthesis approach using a microfluidic-based composition and temperature controlling platform. Front Chem 2020;8.
[33] Global Energy Perspective 2022.
[34] IEA. World energy outlook. 2022. https://www.iea.org/reports/world-energy-outlook-2022.
[35] El-Refaie A, Osama M. High specific power electrical machines: a system perspective. In: CES transactions on electrical machines and systems. 3; 2019. p. 88–93.
[36] Ghassemi M. High power density technologies for large generators and motors for marine applications with focus on electrical insulation challenges. High Volt 2019;5:7–14.
[37] J.B. Bartolo, H. Zhang, D. Gerada, L.D. Lillo, C. Gerada, High speed electrical generators, application, materials and design,.
[38] McHenry ME, Laughlin DE. Magnetic properties of metals and alloys. In: Laughlin DE, Hono K, editors. Physical metallurgy. Oxford: Elsevier; 2014. p. 1881–2008.
[39] Mohn P, Wohlfarth EP. The Curie temperature of the ferromagnetic transition metals and their compounds. J Phys F Met Phys 1987;17:2421.
[40] Mori N. Calculation of ferromagnetic anisotropy energies for Ni and Fe metals. J Phys Soc Jpn 1969;27:307–12.
[41] Chaudhary V, Tan LP, Sharma VK, Ramanujan RV. Accelerated study of magnetic Fe-Co-Ni alloys through compositionally graded spark plasma sintered samples. J Alloys Compd 2021;869:159318.
[42] Bozorth RM. Ferromagnetism. Wiley-IEEE Press; 1993.
[43] ASM Handbook Volume 2: Properties and selection: nonferrous alloys and special purpose materials. ASM International; 1990.
[44] Jen SU, Chiang HP, Chung CM, Kao MN. Magnetic properties of Co–Fe–Ni films. J Magn Magn Mater 2001;236:312–9.
[45] Paganotti A, Bessa CVX, Ferreira LDR, Gama S, Silva RAG. Annealing effect on thermal, mechanical and magnetic properties of Fe–Ni–Co alloys. J Alloys Compd 2019;811:152029.
[46] Special Metals, The NILO® and NILOMAG® Nickel-Iron Alloys, https://www.specialmetals.com/documents/technical-bulletins/nilo-alloys.pdf.
[47] Han L, Maccari F, Souza Filho IR, Peter NJ, Wei Y, Gault B, et al. A mechanically strong and ductile soft magnet with extremely low coercivity. Nature 2022;608:310–6.
[48] E.P. George, Magnetically soft but mechanically tough alloys.
[49] Bott TR, Rassoul GAR. The effects of contact between hydrazine solutions and some polymer materials. Polymer 1970;11:640–6.
[50] Jeon NL, Dertinger SKW, Chiu DT, Choi IS, Stroock AD, Whitesides GM. Generation of solution and surface gradients using microfluidic systems. Langmuir 2000;16:8311–6.
[51] Dertinger SKW, Chiu DT, Jeon NL, Whitesides GM. Generation of gradients having complex shapes using microfluidic networks. Anal Chem 2001;73:1240–6.
[52] Zhang T, Meng J, Li S, Yu C, Li J, Wei C, et al. A microfluidic concentration gradient maker with tunable concentration profiles by changing feed flow rate ratios. Micromachines 2020;11:284.
[53] Toh AGG, Wang ZP, Yang C, Nguyen N-T. Engineering microfluidic concentration gradient generators for biological applications. Microfluid Nanofluidics 2014;16:1–18.
[54] Wang Y-H, Ping C-H, Sun Y-S. Design of christmas-tree-like microfluidic gradient generators for cell-based studies. Chemosensors 2022;11:2.
[55] Shen Q, Zhou Q, Lu Z, Zhang N. Generation of linear and parabolic concentration gradients by using a Christmas tree-shaped microfluidic network. Wuhan Univ J Nat Sci 2018;23:244–50.
[56] Tan LP, Chaudhary V, Tsakadze Z, Ramanujan RV. Rapid multiple property determination from bulk materials libraries prepared from chemically synthesized powders. Sci Rep 2022;12:9504.
[57] Schroder DK. Semiconductor material and device characterization. John Wiley & Sons; 2015.
[58] Tan LP, Padhy SP, Tsakadze Z, Chaudhary V, Ramanujan RV. Accelerated property evaluation of Ni–Co materials libraries produced by multiple processing techniques. J Mater Res Technol 2022;20:4186–96.
[59] Chaudhary V, Sai Kiran Kumar Yadav NM, Mantri SA, Dasari S, Jagetia A, Ramanujan RV, et al. Additive manufacturing of functionally graded Co–Fe and Ni–Fe magnetic materials. J Alloys Compd 2020;823:153817.
[60] Kim S-H, Lee G-H, Park JY, Lee S-H. Microplatforms for gradient field generation of various properties and biological applications. J Lab Autom 2015;20:82–95.
[61] Zaharov YA, Pugachev VM, Ovcharenko VI, Datiy KA, Popova AN, Bogomyakov AS. Phase composition and magnetic properties of nanostructured Fe–Co–Ni powders. Phys Status Solidi B 2018;255:1700175.
[62] Chokprasombat K, Pinitsoontorn S, Maensiri S. Effects of Ni content on nanocrystalline Fe–Co–Ni ternary alloys synthesized by a chemical reduction method. J Magn Magn Mater 2016;405:174–80.
[63] Xu Z, Jin C, Xia A, Zhang J, Zhu G. Structural and magnetic properties of nanocrystalline nickel-rich Fe–Ni alloy powders prepared via hydrazine reduction. J Magn Magn Mater 2013;336:14–9.
[64] Bard A. Standard potentials in aqueous solution. Routledge; 2017.
[65] Billas IML, Châtelain A, de Heer WA. Magnetism from the atom to the bulk in iron, cobalt, and nickel clusters. Science 1994;265:1682–4.
[66] Teh WH, Chaudhary V, Chen S, Lim SH, Wei F, Lee JY, et al. High throughput multi-property evaluation of additively manufactured Co-Fe-Ni materials libraries. Addit Manuf 2022;58:102983.
[67] Moghimi N, Rahsepar FR, Srivastava S, Heinig N, Leung KT. Shape-dependent magnetism of bimetallic FeNi nanosystems. J Mater Chem C 2014;2:6370–5.
[68] Srakaew N, Jantaratana P, Nipakul P, Sirisathitkul C. Structural and magnetic properties of FexNi100−x alloys synthesized using Al as a reducing metal. J Magn Magn Mater 2017;435:201–5.
[69] Chechenin NG, Khomenko EV, de Hosson JTM. FCC/BCC competition and enhancement of saturation magnetization in nanocrystalline Co-Ni-Fe films. JETP Lett 2007;85:212–5.

[70] Hu P, Chen Z-Y, Chang T, Deng J, Yang F, Wang K-S, et al. Magnetic properties of the nanoscale coral-shaped Ni-Co alloy powder with different Co contents. J Alloys Compd 2017;727:332–7.
[71] Dalavi SB, Theerthagiri J, Raja MM, Panda RN. Synthesis, characterization and magnetic properties of nanocrystalline FexNi80−xCo20 ternary alloys. J Magn Magn Mater 2013;344:30–4.
[72] Padhy SP, Tsakadze Z, Chaudhary V, Lim GJ, Tan X, Lew WS, et al. Rapid multi-property assessment of compositionally modulated Fe-Co-Ni thin film material libraries. Results Mater 2022;14:100283.
[73] Leary A, Keylin V, Devaraj A, DeGeorge V, Ohodnicki P, McHenry ME. Stress induced anisotropy in Co-rich magnetic nanocomposites for inductive applications. J Mater Res 2016;31:3089–107.
[74] Cheng M, Wen M, Zhou S, Wu Q, Sun B. Solvothermal synthesis of NiCo alloy icosahedral nanocrystals. Inorg Chem 2012;51:1495–500.
[75] Buravlev IY, Shichalin OO, Papynov EK, Golub AV, Gridasova EA, Buravleva AA, et al. WC-5TiC-10Co hard metal alloy fabrication via mechanochemical and SPS techniques. Int J Refract Metals Hard Mater 2021;94:105385.
[76] Shichalin OO, Buravlev IY, Portnyagin AS, Dvornik MI, Mikhailenko EA, Golub AV, et al. SPS hard metal alloy WC-8Ni-8Fe fabrication based on mechanochemical synthetic tungsten carbide powder. J Alloys Compd 2020;816:152547.
[77] Shichalin OO, Buravlev IY, Papynov EK, Golub AV, Belov AA, Buravleva AA, et al. Comparative study of WC-based hard alloys fabrication via spark plasma sintering using Co, Fe, Ni, Cr, and Ti binders. Int J Refract Metals Hard Mater 2022;102:105725.
[78] Shichalin OO, Papynov EK, Buravlev IY, Buravleva AA, Chuklinov SV, Gridasova EA, et al. Functionally gradient material fabrication based on Cr, Ti, Fe, Ni, Co, Cu metal layers via spark plasma sintering. Coatings 2023;13:138.
[79] Li C, Ruan H, Chen D, Li K, Guo D, Shao B. Effect of heat treatment on the microstructure and properties of Ni based soft magnetic alloy. Microsc Res Tech 2018;81:796–802.
[80] Osaka T, Takai M, Hayashi K, Ohashi K, Saito M, Yamada K. A soft magnetic CoNiFe film with high saturation magnetic flux density and low coercivity. Nature 1998;392:796–8.